Regulating Li-Ion Transport through Ultrathin Molecular Membrane to Enable High-Performance All-Solid-State–Battery

Sathish Rajendran, Antony George, Zian Tang, Christof Neumann, Andrey Turchanin,* and Leela Mohana Reddy Arava*

Solid-state lithium metal batteries with garnet-type electrolyte provide several advantages over conventional lithium-ion batteries, especially for safety and energy density. However, a few grand challenges such as the propagation of Li dendrites, poor interfacial contact between the solid electrolyte and the electrodes, and formation of lithium carbonate during ambient exposure over the solid-state electrolyte prevent the viability of such batteries. Herein, an ultrathin sub-nanometer porous carbon nanomembrane (CNM) is employed on the surface of solid-state electrolyte (SSE) that increases the adhesion of SSE with electrodes, prevents lithium carbonate formation over the surface, regulates the flow of Li-ions, and blocks any electronic leakage. The sub-nanometer scale pores in CNM allow rapid permeation of Li-ions across the electrode–electrolyte interface without the presence of any liquid medium. Additionally, CNM suppresses the propagation of Li dendrites by over sevenfold up to a current density of 0.7 mA cm^{-2} and enables the cycling of all-solid-state batteries at low stack pressure of 2 MPa using LiFePO$_4$ cathode and Li metal anode. The CNM provides chemical stability to the solid electrolyte for over 4 weeks of ambient exposure with less than a 4% increase in surface impurities.

S. Rajendran, L. M. R. Arava
Department of Mechanical Engineering
Wayne State University
Detroit, MI 48202, USA
E-mail: leela.arava@wayne.edu
A. George, Z. Tang, C. Neumann, A. Turchanin
Institute of Physical Chemistry
Friedrich Schiller University Jena
07743 Jena, Germany
E-mail: andrey.turchanin@uni-jena.de
A. Turchanin
Center for Energy and Environmental Chemistry Jena (CEEC Jena)
07743 Jena, Germany

1. Introduction

An increase in the demand for electric vehicles and portable electronics pushes the need for advanced energy storage technologies. Li metal batteries are an attractive option that provides high energy density because Li metal anode possesses the highest theoretical specific capacity of 3860 mAh g^{-1} and lowest reduction potential (−3.04 V vs standard hydrogen electrode).[1] However, Li metal batteries are limited by the safety hazards they impose due to the use of organic liquid electrolytes, which have low flash points leading to the risk of fire and explosion.[2] Replacing the liquid electrolyte with an inorganic solid-state electrolyte (SSE) provides higher safety due to the absence of flammable components, and high energy density to meet the needs of the future.[3]

The past 10–15 years marked the development of fast Li-ion conducting SSEs that have almost achieved a Li-ion conductivity close to that of liquid electrolytes (10^{-2} to 10^{-3} S cm^{-1} at room temperature).[3a,4] Among various Li-ion conductors, garnet-type SSEs have obtained considerable attention due to their high Li-ion conductivity, stability with Li metal, and wide electrochemical stability window.[5] Despite obtaining fast Li-ion conduction, these electrolytes fail to achieve considerable performance when employed in a full cell due to multiple issues associated with the solid–solid interfaces between the electrodes and the SSE.[6] Another major challenge lies in the propagation of Li dendrites through the SSE, which is again partially associated with the solid–solid interface.[7] Garnets are rigid ceramic materials that possess almost zero elasticity.[8] Due to this reason, the SSE cannot cope with the volume expansion and contraction of the anode and cathode during the charge–discharge cycles.[9] This leads to a loss in contact between the electrodes and the SSE that increases the polarization and reduces the capacity. This loss in electrode–electrolyte contact area at certain locations increases the effective current density on the region in contact that results in the propagation of Li dendrites. Relatively higher electronic conductivity of garnet-type SSE has also been claimed as one of the reasons for the propagation of Li dendrites.[10] The direct contact of Li anode with the cubic phase

**ADVANCED
SCIENCE NEWS**

www.advancedsciencenews.com

**NANO · MICRO
small**

www.small-journal.com

of garnet was found to convert a few unit cells of cubic phase to the tetragonal phase that possesses lower Li-ion conductivity.[11] Garnets were also found to be highly reactive with moisture and carbon dioxide during ambient atmosphere. This leads to the formation of Li_2CO_3, which has poor wettability with molten Li.[12] On the cathode side, the difference in chemical potential leads to the formation of a space charge layer that obstructs the flow of Li-ions across the interface.[13] Hence, the next step in developing better all-solid-state batteries (ASSBs) lies in the integration of solid–solid interfaces.[6]

Herein, we address the multiple issues associated with garnet-type SSE with a concept of cation regulation using a 2D ultra-thin (≈ 1 nm) polymeric carbon nanomembrane (CNM).[14] The CNM provides high flexibility for the integration of cathodes with the SSE and regulates the diffusion of Li-ions across the interface, which plays a prominent role in the suppression of Li dendrites. The CNMs fabrication involves cross-linking of self-assembled monolayers (SAMs) using electron beam irradiation.[15] The molecular gaps between cross-linked molecules act as pores for the Li-ion permeation. The molecular gaps possess a pore size of ≈ 0.6–0.7 nm,[16] which is about approximately ten times higher than the size of Li–ion, and a pore density of 10^{14} cm^{-2} that regulates the Li-ion mass transport at the interface as discussed in detail in our previous work.[17] A systematic investigation of the role of CNMs in ASSBs has been elucidated through spectroscopic, microscopic, and electrochemical studies. Further, the synthesis and transfer of CNM to the SSE is scalable to a large scale that promises better performing batteries of all form factors. Employing such sub-nanochannels have been proven effective on suppressing lithium dendrites in conventional Li-ion batteries;[17] and is a first-of-its-kind application in ASSBs.

2. Results and Discussion

2.1. LLZT Characterization

Tantalum (Ta) doped $Li_7La_3Zr_2O_{12}$ with nominal composition $Li_{6.4}La_3Zr_{1.4}Ta_{0.6}O_{12}$ (LLZT) was synthesized through conventional solid-state synthesis. The supervalent Ta^{5+} cation occupies the 16a site along with Zr^{4+} imparting cubic phase stability and slightly higher conductivity by creating vacancies in the crystal lattice. The composition is abbreviated as LLZT for this entire study. The successful formation of the cubic phase was confirmed by X-ray diffraction (XRD) analysis, as shown in Figure S1, Supporting Information. Rietveld refinement of the XRD data was conducted based on a similar composition available in the open crystallography database. The final Rietveld refinement pattern fitted well with the XRD data with a good R_{wp} factor of 8.18%. This correspondence confirms the formation of the cubic phase with the Ia-3d space group. The unit cell parameter a was found to be 12.8521 Å, which is in good agreement with the literature values of 12.9101[18] and 12.9455 Å.[19] It is also to be noted that there was not any detection of other common impurity phases such as Li_2CO_3, $LiAlO_3$, and Li_6ZrO_7. The ionic conductivity measurements were carried out using electrochemical impedance spectroscopy (EIS) on LLZT attached with blocking electrodes (silver) at various temperatures, as shown in Figure S2a, Supporting Information. As evident from the plot, the semicircle corresponding to the bulk resistance and grain boundary resistance was only

observed at lower temperatures. With an increase in temperature, only the low-frequency line corresponding to the blocking electrodes was observed. This phenomenon is due to the increasing relaxation frequency, $\omega = 1/RC$, of the LLZT bulk, which changes due to the temperature dependence on resistance.[20] To overcome this issue, a high-frequency analyzer capable of measuring EIS at high frequencies ≈ 40 MHz is required, and most laboratory impedance analyzers are limited to 7 MHz. The bulk resistance value was obtained from curve fitting the EIS spectra using the equivalent circuit $R_1/CPE_1 + CPE_2 + L_1$, where R_1 is the bulk resistance, CPE stands for the constant phase element, and L stands for the inductor. The ionic conductivity was calculated using Equation (1), where R is the bulk resistance, l is the thickness of the pellet, and A is the area of the pellet.[20]

$$\sigma_{bulk} = \frac{1}{R} \times \frac{l}{A} \tag{1}$$

The ionic conductivity values measured at various temperatures were plotted in the form of an Arrhenius plot, as shown in Figure S2b, Supporting Information. It is observed from the straight-line slope that it follows typical Arrhenius behavior, which can be expressed by Equation (2), where A is the pre-exponential factor, E_a is the activation energy, k is the Boltzmann constant, and T is the temperature.

$$\sigma = \frac{A}{T} \exp\left(\frac{-E_a}{kT}\right) \tag{2}$$

The ionic conductivity of the LLZT was calculated to be 1.13×10^{-4} S cm^{-1} at room temperature and the activation energy was calculated to be 0.314 eV. The obtained values were coherent with the literature values.[21] To analyze the microstructure of the LLZT pellet, field emission scanning electron microscopy (FE-SEM) analysis along the fracture cross-section was carried out, as shown in Figure S3, Supporting Information. The FE-SEM image shows a dense electrolyte with an average grain size of 12 μm. A few voids and defect sites were also present, which is unavoidable during the conventional sintering process. The relative density of the LLZT pellet was calculated to be 90.3% considering the theoretical density of LLZT to be 5.491 g cm^{-3}. Soon after the polishing step of the LLZT pellet, the sample was transferred to an X-ray photoelectron spectroscopy (XPS) vacuum transfer module to prevent any surface degradation. It is to be noted that LLZT is highly reactive with the atmosphere to form Li_2CO_3 with just a few minutes of exposure to the ambient atmosphere.[22] The LLZT pellet was loaded into the XPS chamber for analysis, and the results are shown in Figure S4, Supporting Information. The C 1s spectrum (Figure S4a, Supporting Information) is composed of multiple components, including the adventitious carbon peak at 285.0 eV. The peaks at 286.6 $\pm$ 0.2 and 288.6 $\pm$ 0.1 eV correspond to the presence of impurities containing C–O and O=C–O functional groups, respectively.[23] The presence of Li_2CO_3 contaminant at $\approx 290.0 \pm 0.2$ eV was detected, which proves that surface contamination by Li_2CO_3 is almost inevitable by dry polishing techniques.[22,24] A partial reason for this contamination is the requirement of ambient conditions for the synthesis of the oxide-type LLZT electrolytes. The Zr 3d spectra in Figure S4b, Supporting Information, and La 3d spectra
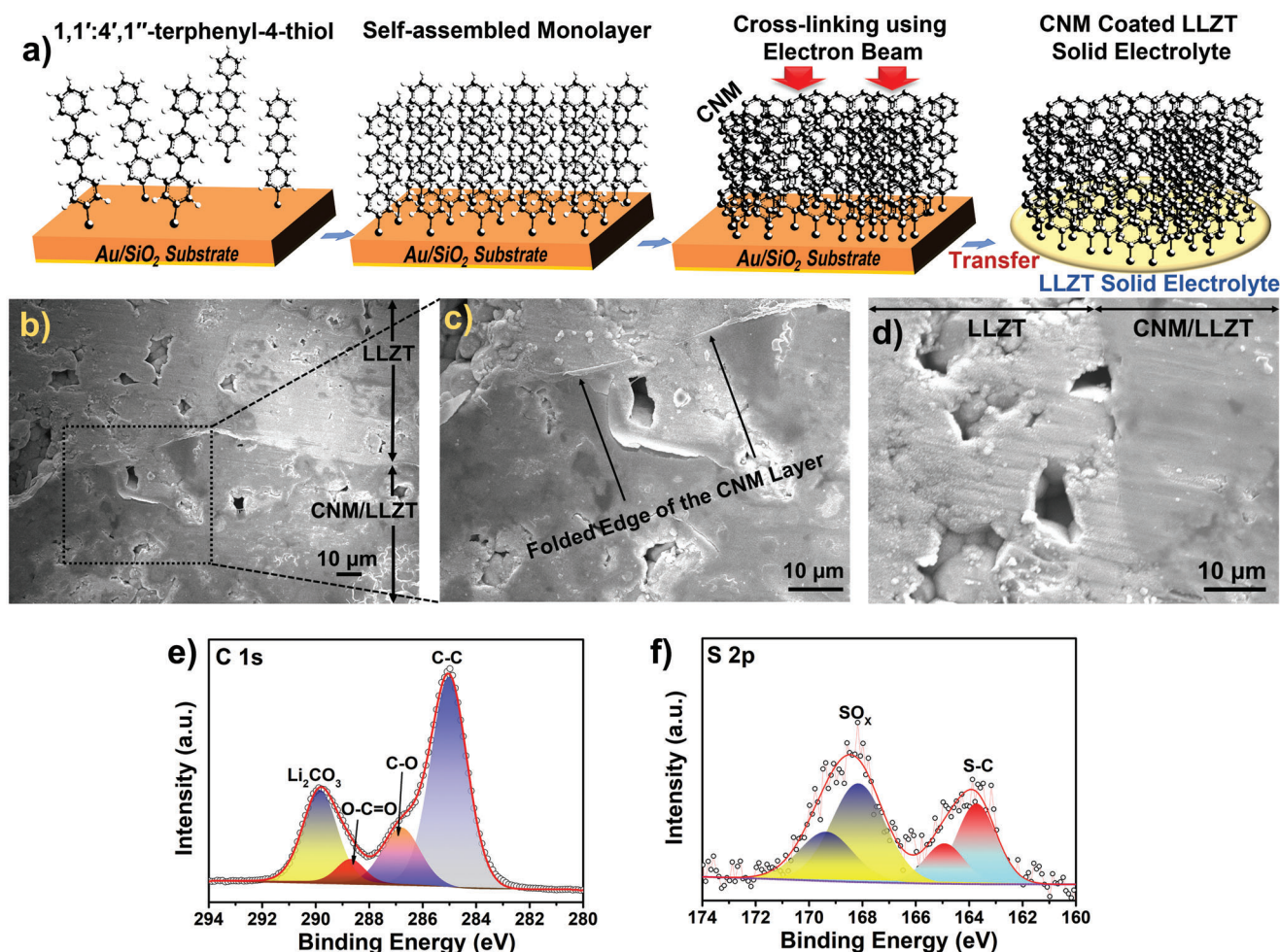
ADVANCED
SCIENCE NEWS
www.advancedsciencenews.com

NANO · MICRO
small
www.small-journal.com

Figure 1. a) Schematic of the synthesis and transfer of CNM from 1,1′:4′,1″-terphenyl-4-thiol molecules onto the LLZT solid electrolyte, b–d) FE-SEM images of the CNM coated LLZT pellet at different magnifications, e) C 1s and f) S 2p XP spectra of CNM/LLZT.

in Figure S4c, Supporting Information, show weak Zr and La signals which are due to the masking of the features by the surface contaminants.[23] The O 1s spectrum in Figure S4d, Supporting Information, shows a major peak at ≈531.5 eV and a minor peak at ≈528.7 eV. The minor peak corresponds to the O^{2-} in the LLZT lattice and the major peak corresponds to the O–C bond present in the surface Li_2CO_3 layer.[25] This phenomenon is common in LLZT with even a very insignificant level of surface impurity because of the exponential decay of the intensity due to the masking effect.[23] From the above characterizations, it is evident that LLZT was successfully synthesized and a very small inevitable amount of Li_2CO_3 surface remained on the surface of the LLZT electrolyte pellet.

2.2. CNM Characterization on LLZT

The fundamental building block of the CNM is the 1,1′:4′,1″-terphenyl-4-thiol (TPT) molecule consisting of a thiol group at one end followed by three conjugated phenyl rings. The series of steps to obtain a TPT CNM is shown in **Figure 1**a. The first step involves the deposition of TPT molecules on an Au/SiO₂

substrate to form an SAM of TPT molecules. Despite containing conjugated rings in the TPT molecule, the electrical resistance of the formed SAM was found to be 10^8 Ω when aligned in the perpendicular direction.[26] Subsequent steps involve cross-linking of the aligned TPT molecules using a low-energy electron beam to form the CNM. By irradiating electrons, the TPT molecules cross-link forming an even more insulating CNM.[27] In the last step, the formed CNM on the Au/SiO₂ substrate is transferred to the LLZT solid electrolyte through electrochemical delamination assisted transfer.[28] The CNM-transferred LLZT solid electrolyte is hereafter referred to as CNM/LLZT and the electrolyte without the CNM is referred to as LLZT. The CNM/LLZT was analyzed through FE-SEM, as shown in Figure 1b–d. In all three images, the region with CNM could be clearly identified. The CNM was found to be highly uniform without any blisters and tears (Figure 1b). Magnified image (Figure 1c) shows the curled edges of the CNM as observed on other substrates as well.[17] The CNM was found to be absent in the region above large defect sites >2 µm (unavoidable in conventional sintering), which is due to the inability of ultra-thin nanostructures to hang freely above vacant sites. Figure 1d shows the FE-SEM image after sputter coating the sample with a layer of gold (about 80 to 100 nm). The

**ADVANCED
SCIENCE NEWS**

www.advancedsciencenews.com

**NANO · MICRO
small**

www.small-journal.com

contrast of the CNM on the LLZT is enhanced due to the thick gold layer confirming their uniformity. The CNM spreads over the LLZT like a sheet of separator that is capable of permeating Li-ions. The permeation of Li-ion through the TPT-CNM membrane is studied separately by sandwiching the CNM in-between two Li-ion conducting polyethylene oxide layers that is further in contact with Li-metal.[29] The areal Li-ion conductivity for the TPT-CNM was found to be ≈0.5 mS cm^{-2} at room temperature, which indicates the ultra-fast permeation of Li-ion. The digital image of the gold sputtered sample is known in Figure S5, Supporting Information, which clearly shows two distinctive regions. The region covered with the CNM is shiny in nature because of the smooth topography caused by the CNM membrane. On the other hand, the gold sputtered LLZT surface is dull in color because of the high surface roughness of the ceramic solid electrolyte. Overall, the CNM was found to be highly adherent and uniformly spread over the LLZT surface. The chemical integrity of the CNM was confirmed using XPS analysis of the CNM/LLZT. The C 1s spectrum shows distinctive peaks at 285.0, 286.6 ± 0.2, 288.7 ± 0.1, and 290 ± 0.2 eV corresponding to adventitious carbon (C–C), alkoxide surface impurities from atmosphere, carboxyl impurity from a small amount of residual poly(methyl methacrylate) (PMMA), and lithium carbonate present on the LLZT surface, respectively. The intensity of the lithium carbonate peak increased when compared to the LLZT before CNM transfer (Figure S4, Supporting Information), which stems from further accumulation of Li_2CO_3 layer during the CNM transfer process in an open atmosphere. The core level S 2p spectrum shows two doublets according to spin orbit splitting. The first set of doublet peaks at 163.7 ± 0.1 and 164.9 ± 0.1 eV correspond to the S 2p$_{3/2}$ and S 2p$_{1/2}$ peaks of the S–C bonds present in the CNM. This confirms the successful transfer of the CNM onto the LLZT. Apart from S–C doublet, a set of doublet peaks at 168.1 ± 0.2 and 169.3 ± 0.2 eV corresponding to the partially oxidized sulfur (SO$_x$) was also present. This species is related to the oxidation of some of the thiol groups during electrochemically assisted transfer as observed in the previously reported results.[17,28]

2.3. Prevention of Lithium Carbonate Formation over LLZT Using CNM

Storage and material processibility at ambient conditions of the solid-state electrolytes are essential for large-scale manufacturing. The surface of the LLZT reacts with moisture and CO_2 to form Li_2CO_3.[25] The formed Li_2CO_3 has poor adhesion with Li metal that in turn ends up in high interfacial resistance. An ideal solution will be a one-step engineering approach that can prevent lithium carbonate formation, dendrites, and provide adhesion to the LLZT solid electrolyte. To prevent lithium carbonate formation, the CNM should ideally block the permeation of gases into the surface of the LLZT. Despite CNM being permeable to water, it requires a driving force such as a pressure difference for the water molecules to move across the membrane.[30] Further, the rate of permittivity of CO_2 is five orders (10^5) lower than moisture.[31] Herein, to analyze if the CNM layer would prevent the contact of LLZT to atmospheric exposure, XPS measurements were recorded before and after exposing the pellets to an open atmosphere for 4 weeks. The C 1s spectrum of the dry polished LLZT electrolyte is shown in **Figure 2**a. The ratio of the Li_2CO_3 peak intensity to the adventitious carbon intensity was about 0.50 ± 0.04. After atmospheric exposure (Figure 2b), the peak corresponding to the Li_2CO_3 evolved drastically indicating the rate of formation of the surface impurity layer over the LLZT surface and the peaks intensity ratio was found to be about 1.50 ± 0.02. Along with Li_2CO_3, the carboxyl impurity (COO$^-$) peak also evolved with a substantial amount. Such observation of an increase in carboxyl peak during atmospheric exposure is in accordance with the previous literature.[22,32] In the case of CNM/LLZT, the ratio of the intensity and adventitious carbon on a fresh sample was found to be about 0.50 ± 0.01. After 4 weeks of atmospheric exposure, the intensity of both carbonate and adventitious carbon peaks increased only by ≈10%, which may be because of point-to-point variation in the same sample or a very negligible amount of carbonate accumulation over the defect sites of CNM/LLZT. The ratio of the peak intensities was found to be the same as the fresh sample at about 0.50 ± 0.01. Hence, the increase in carbonate species is negligible over the surface of the CNM/LLZT, which solidifies the fact that the CNM layer protects the LLZT solid electrolyte from ambient exposure induced degradation. Figure 2e shows the FE-SEM image of the CNM/LLZT pellet after 4 weeks of atmospheric exposure. The region without the CNM had surface species adsorbed over the LLZT that corresponds to the Li_2CO_3 formation over LLZT, which fills the defect sites of the LLZT and hinders the view of the grain microstructure of the LLZT. Contrary to the observed result on LLZT, the impurities on the solid electrolyte surface are absent while the microstructure of the grains is still distinct in the regions covered with CNM. This observation supports the XPS result where the CNM prevents the formation of Li_2CO_3 over LLZT.

2.4. Adhesion of LLZT with Li Metal

The key challenge for a solid-state battery is to achieve smooth transfer of Li-ions across the electrode–electrolyte (solid–solid) interfaces. An important factor governing this transfer is the adhesion of the Li metal on the LLZT solid electrolyte, which minimizes the interfacial resistance for Li-ion transport. The interaction of molten Li with LLZT is shown in **Figure 3**a. The molten Li tends to roll away from the LLZT surface and stick to the sides of the LLZT pellet or the stainless-steel container. Adding a larger quantity of molten Li results in a chunky ball formation over the LLZT surface (Figure S6a, Supporting Information). Figure 3b,c shows the FE-SEM cross-sectional image after heating the LLZT along with a Li foil at 180 °C for 2 h. Only a limited area of LLZT could get in contact with the Li metal and the majority of the area possesses voids that are not in contact with Li metal. The sporadic contact of Li metal over the LLZT will end up in high interfacial resistance that impacts the transfer of Li-ions across the interface. Apart from the interfacial resistance, the amount of current flowing through the area will be several orders higher than the calculated areal current density, which will promote the formation of Li dendrites. The interaction between LLZT and molten Li is better portrayed in Video S1, Supporting Information, and its screen shots in Figure S7, Supporting Information. As the LLZT pellet is dipped and taken out from molten Li, there are no signs of adhesion
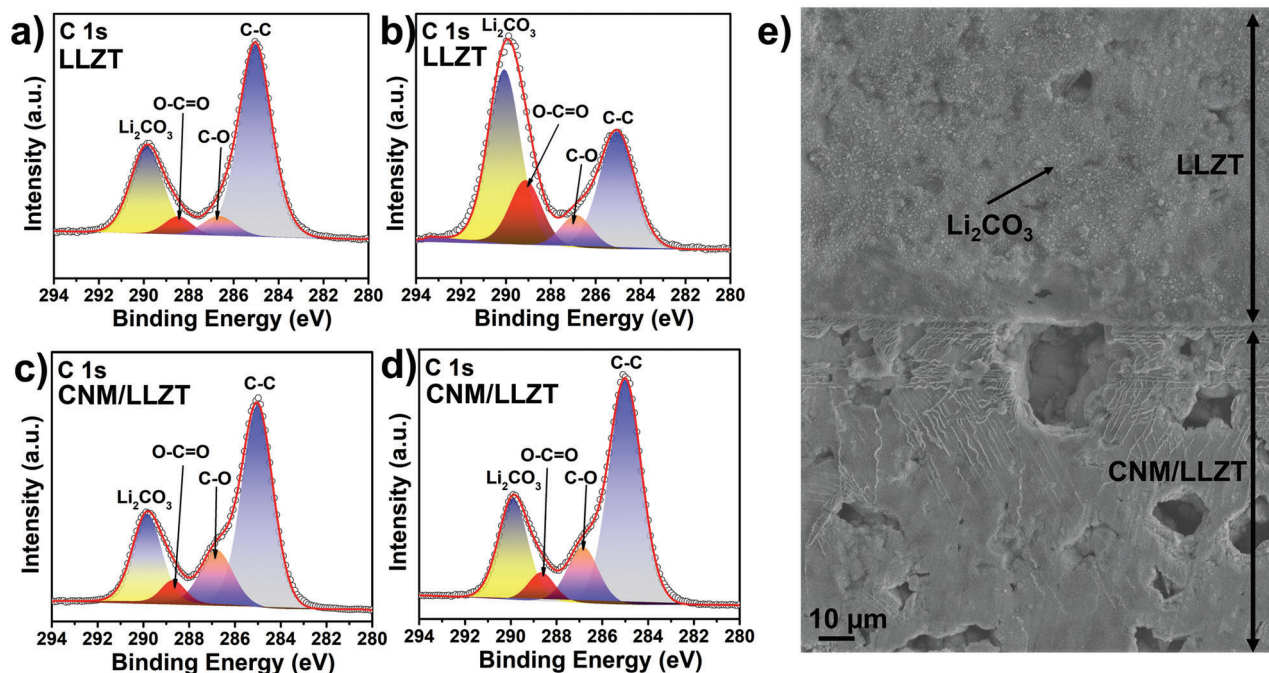
ADVANCED
SCIENCE NEWS
www.advancedsciencenews.com

NANO · MICRO
small
www.small-journal.com

Figure 2. a–d) High resolution C 1s XP spectra of a,b) LLZT and c,d) CNM/LLZT measured a,c) before and b,d) after aging in a closed container with room atmosphere for 4 weeks and e) FE-SEM image of CNM/LLZT after the aging studies.

of Li over the LLZT surface. The non-adhesive nature of LLZT is from the surface Li_2CO_3 layer that has poor adhesion with Li metal. On the other hand, the interaction between molten Li and CNM/LLZT is shown in Figure 3d. The molten Li adheres well with the CNM/LLZT pellet despite the presence of the surface Li_2CO_3 layer over the LLZT surface. This adhesion behavior can only be possible when the nanometer thick CNM is highly adherent with the LLZT and with Li metal. The superior mechanical properties of the CNM prevents it from rupturing.[33] The adhesion was also tested with an additional quantity of molten Li (Figure S6b,c, Supporting Information) and the CNM/LLZT surface was quite in contact with Li, unlike the globule formation

observed in the case of LLZT. The FE-SEM cross-sectional image after heating the Li foil and CNM/LLZT at 180 °C for 2 h is shown in Figure 3e,f. The Li foil is highly adherent over the CNM/LLZT pellet with no defects or discontinuities over the interface. Such uniform interfaces aid the suppression of dendrite formation. Further, the CNM is highly electronically insulating in nature that ideally prevents any electronic leakage into the solid electrolyte. Video S2 and Figure S7, Supporting Information, show the interaction between molten Li and CNM/LLZT. As soon as the CNM/LLZT pellet in inserted into the pool of molten Li, the corresponding CNM/LLZT surface adheres to the molten Li as it is retracted out.
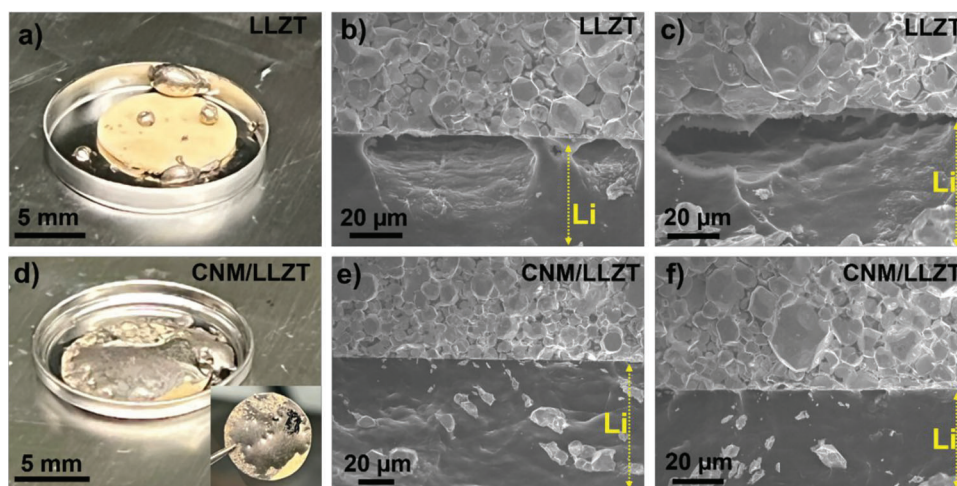

Figure 3. a,d) Digital images and b,c,e,f) FE-SEM images of molten Li wettability on a–c) LLZT and d–f) CNM/LLZT.
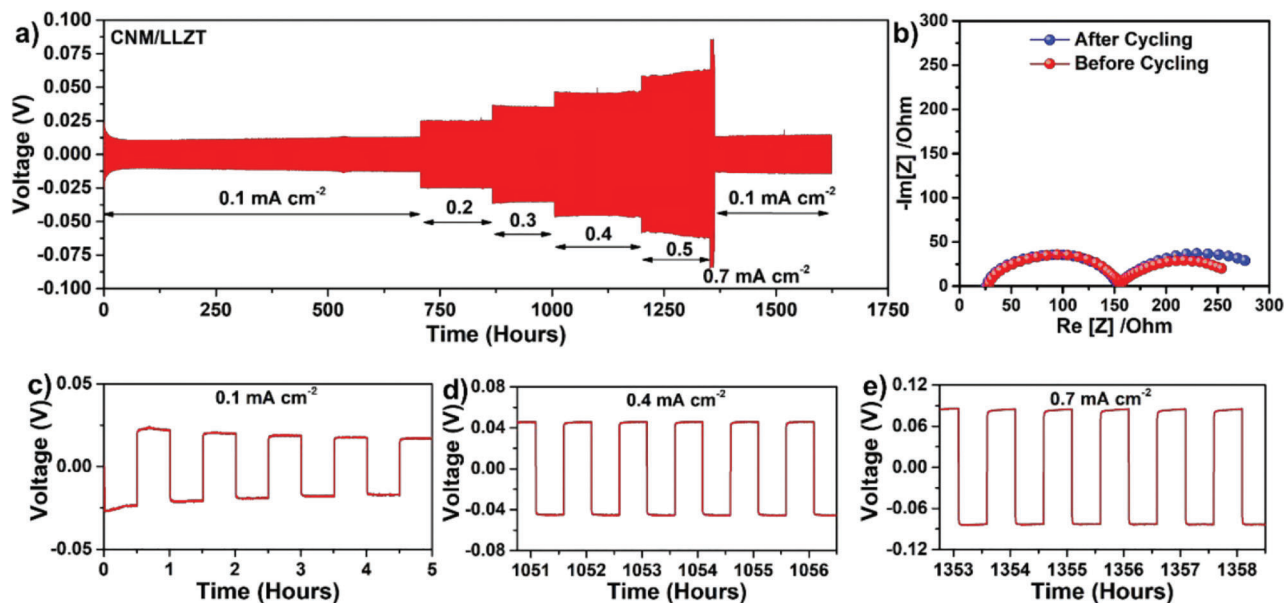
Figure 4. a) Galvanostatic cycling of the symmetrical cell using CNM/LLZT at various current density ranging from 0.1 to 0.7 mA cm^{-2} at 60 °C; b) corresponding EIS measured before and after cycling. Zoomed part of the galvanostatic cycling at c) 0.1, d) 0.4, and e) 0.7 mA cm^{-2}.

2.5. Dendrites and Interfacial Resistance Evaluation Using Symmetrical Cell

To observe the effect of the adherent, cation regulating CNM/LLZT interface with Li metal, a symmetric cell with CNM/LLZT sandwiched in-between two Li foils on either side was fabricated and tested at 60 °C. The temperature, 60 °C, was chosen as the optimum level for the study to achieve reasonable ionic conductivity in the LLZT electrolyte. The operating temperature can be lowered by making defect free solid electrolytes through advanced sintering techniques.[34] Li plating and stripping tests were done at different current densities, as shown in **Figure 4**a. The EIS was recorded before and after cycling the symmetrical cells as shown in Figure 4b. The interfacial resistance of the Li-CNM/LLZT interface was calculated by fitting the EIS and was found to be 54 Ω cm^2 before cycling of the symmetric cell. The value matches with the one obtained using Ohm's law (51.5 Ω cm^2) from the DC polarization in the initial few seconds of cycling. After a few minutes of cycling, the interfacial resistance of the Li-CNM/LLZT interface reduced to 10.3 Ω cm^2 as observed from the polarization in the Li plating/stripping curve (Figure 4a). The decrease in the interfacial resistance signifies the creation of an adherent contact in the initial few minutes of cycling. This can also be from the interaction of Li metal anode with the thiol group to form a Li–S bond in the interface as observed previously when CNM was employed in conventional Li-ion batteries.[17] The symmetric cell exhibited stable cycling at various current densities (Figure 4d,e). The cell polarization appeared to increase by a margin at current densities of 0.5 and 0.7 mA cm^{-2}. At 0.7 mA cm^{-2} the voltage profile appeared to deviate from the typical square wave profile observed at other current densities (Figure 4e). However, when switched back to 0.1 mA cm^{-2}, the symmetric cell exhibited stable cycling with perfect square wave profile. After 1620 h of cycling at different current densities, the interfacial resistance was found to be 69 Ω cm^2, obtained from the EIS in Figure 4b. The slight increase in the interfacial impedance after cycling may be the result of high current density cycling, especially at 0.5 and 0.7 mA cm^{-2}, where the cell polarization was found to increase with time. Without the CNM, the LLZT solid electrolyte has very poor adhesion with Li metal and exhibits very poor symmetric cell performance even at low current density (0.2 mA cm^{-2}) as shown in our previous work with similar experimental conditions at 60 °C.[22] The cell polarization was found to be several orders higher than what was observed in the case of CNM/LLZT. The superior performance of the CNM/LLZT could be from the synergic effect of uniform contact between the Li metal and the solid electrolyte as well as the effect of CNM in regulating the flow of Li-ions into the SSE. To dissect the effect of observed performance in CNM/LLZT, a symmetric cell using a hybrid electrolyte configuration was made using liquid electrolyte that will ensure uniform contact between the LLZT and Li metal. Hybrid electrolyte systems have been the recent solution to solve various interfacial issues in solid state batteries.[35] As shown in Figure S8, Supporting Information, the symmetric cell Li plating/stripping experiment revealed stable cycling at 0.1 mA cm^{-2} with a stable cell polarization of 80.2 mV. However, the cell shorted soon after increasing the current density to 0.2 mA cm^{-2}. Hence, the superior performance in the case of CNM/LLZT is not only from the adherent contact in-between the LLZT and Li metal, but also from the CNM itself. The CNM effectively regulated the flow of Li-ions into the solid electrolyte and essentially controls the Li-ion flux in a particular region. The Li-ion flux will be uniform (homogeneous) across the solid electrolyte and prevents any heavy in-flow of Li-ions in one particular region that may induce Li dendrites. Further, the formed insulating CNM prevents the electronic leakage into the solid electrolyte that will limit the availability of electrons inside the LLZT which will further decimate the reduction of Li-ion to Li metal in the solid-electrolyte's grain boundaries.[3b]
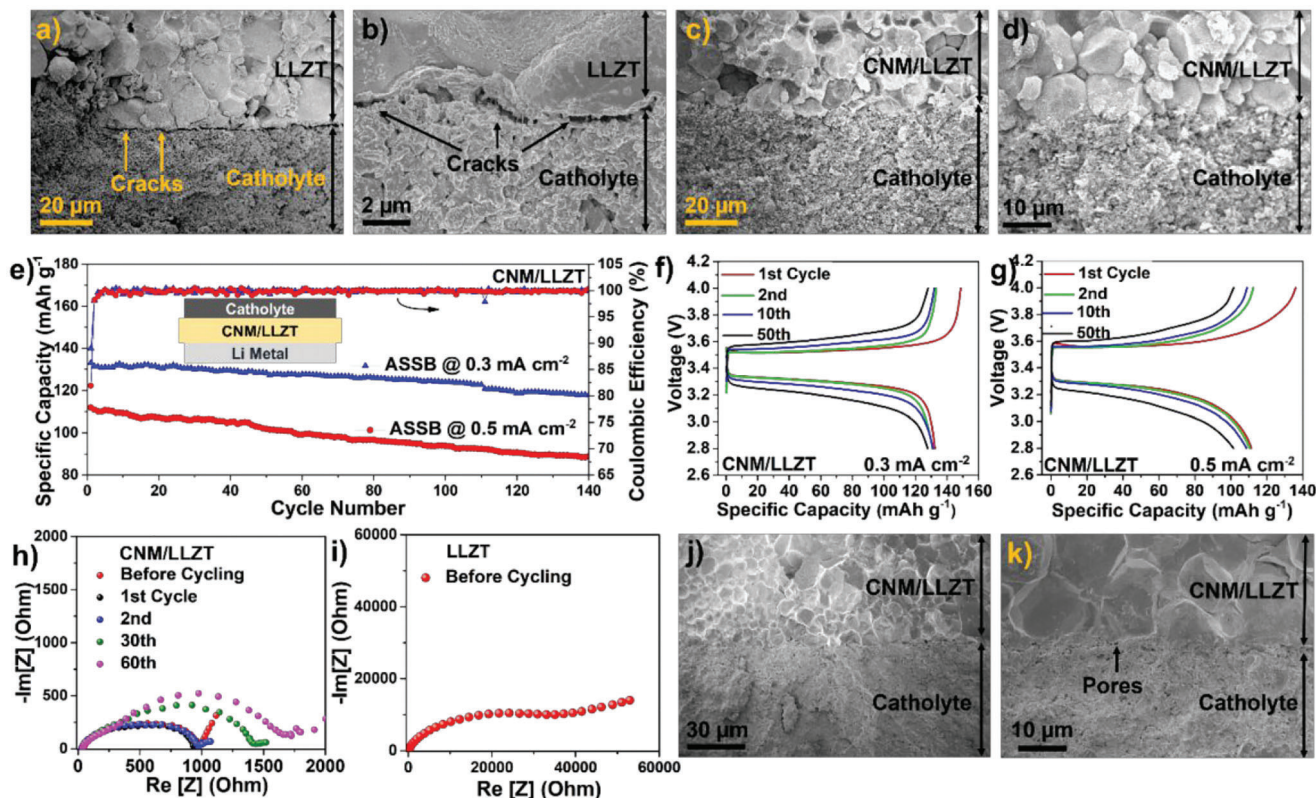
ADVANCED
SCIENCE NEWS
www.advancedsciencenews.com

NANO · MICRO
small
www.small-journal.com

Figure 5. FE-SEM cross-section images of SSE-catholyte interface using a,b) LLZT and c,d) CNM/LLZT at different magnifications; e) Galvanostatic cycling of full cell using LiFePO$_4$ cathode at 0.3 and 0.5 mA cm^{-2} at 60 °C and the corresponding voltage profile of the cell cycled at f) 0.3 and g) 0.5 mA cm^{-2}. EIS evolution during full cell cycling of h) CNM/LLZT and i) LLZT. j,k) FE-SEM cross-section images of cycled cell at 0.3 mA cm^{-2}.

2.6. ASSB Full Cell Performance and Failure Analysis

After obtaining stable cycling performance in the symmetric cell level, full cell studies using LiFePO$_4$ (LFP) cathode were carried out. LFP was chosen as the active material among various cathodes available in the market because of its superior stability at elevated temperatures. The catholyte consists of 60% LFP, 20% LLZT (particle size 650 nm), 15% C-65 conducting carbon, and 5% polyvinylidene difluoride (PVDF) binder. FE-SEM cross-sectional image of catholyte coated over LLZT is shown in **Figure 5**a,b. The adhesion of the catholyte with the solid electrolyte depends on the binder-SSE interaction. As a result of poor adhesion of PVDF binder with the SSE, a gap of about 1 µm is formed in between the catholyte and the SSE (Figure 5a,b). In the case of CNM/LLZT, as shown in Figure 5c,d, the polymeric binders adhere well with the CNM/LLZT, and an adherent interface is formed in between the catholyte and the SSE over the entire region. The electrochemical cycling of the full cell was carried out at two different current densities, 0.3 and 0.5 mA cm^{-2}, as shown in Figure 5e. At 0.3 mA cm^{-2} the cell exhibited an initial capacity of 133 and 116 mAh g^{-1} in the 140th cycle with a capacity loss of 12.7% over 140 cycles. At 0.5 mA cm^{-2}, the cell exhibited a capacity of 111 and 85 mAh g^{-1} in the first and 140th cycle, respectively, which accounts to about 20.7% capacity loss. The coulombic efficiency of both the cells were low in the first cycle (89% and 81%) and found to be close to 100% during the subsequent cycles. The average coulombic efficiency from the

second to 140th cycle was found to be 99.84% and 99.82% for the cells cycled at 0.3 and 0.5 mA cm^{-2}, respectively. The high coulombic efficiency represents the reversible cycling of the full cell without the formation of Li deposits inside the SSE. The voltage profiles of the cell cycled at both current densities are shown in Figure 5f,g. The cell at 0.3 mA cm^{-2} exhibited a cell polarization (difference between cathodic and anodic voltage at mid capacity) of 218 mV in the first cycle and 415 mV in the 50th cycle. The cell at 0.5 mA cm^{-2} exhibited a polarization of 298 mV during the first cycle and 490 mV during the 50th cycle. The high polarization values are due to the high current density applied to the cell and the poor conductivity of the catholyte. 0.5 mA cm^{-2} current density corresponds to about C/2 rate with the catholyte loading used in this work. Although achieving C/2 rate might be easy for conventional Li-ion batteries, it is quite challenging for SSBs involving ceramic electrolyte as it is impeded by several challenges. The specific capacity of the catholyte was found to decrease drastically while the current density was increased, which can be attributed to the porosity of the catholyte that blocks the fast ion transport across the electrode. A dense dry electrode technology with high Li-ion and electron transport is necessary for developing solid-state batteries. Most solid-state battery cycling in literature is done at non-practical stack pressures and possesses very poor cycle life. The reason for the increase in polarization of the full cell was investigated from the EIS analysis of the cell cycled at 0.3 mA cm^{-2} at intermittent cycles, as shown in Figure 5h. The cell impedance before cycling was found to

be 980 Ω from the charge transfer resistance in the EIS. After the first, second, 30th, and 50th cycles, the cell impedance was found to be 943, 964, 1409, and 1671 Ω, respectively. The full cell impedance will have contributions from the charge transfer resistance through the bulk of the solid electrolyte, anode-SSE interface, and the catholyte-SSE interface. From the symmetric cell studies shown in the previous section, the interfacial impedance evolution from the anode-SSE interface is very minimal and is comparatively way less than what is observed here. As seen from the EIS (Figure 5h), the initial portion of the Nyquist plot is overlapping with each other, which confirms the charge transfer resistance through the SSE remains constant throughout the cycling. The increase in cell resistance could only rise from the catholyte-SSE interfacial resistance. To verify this, cross-sectional FE-SEM images of the 0.3 mA cm^{-2} cell after the cycling studies were carried out, as shown in Figure 5j,k. The formation of tiny cracks and pores along the CNM/LLZT and the catholyte interface was observed, which might lead to an increase in resistance for the Li-ion transport across the interface and finally results in enhanced cell polarization. Despite such defect formation at specific sites, rest of the area was adherent to the catholyte unlike the LLZT electrolyte (Figure 5a,b). Such pore formation can be avoided by increasing the stack pressure of the testing or by moving to a hybrid electrolyte architecture using non-flammable liquid electrolytes. To validate the above-mentioned claim, a hybrid electrolyte architecture utilizing room temperature ionic liquid electrolyte (RTIL) was made. The RTIL used in this study was 1-butyl-1-methylpyrrolidinium bis(trifluoromethyl sulfonyl)imide with 1 M lithium bis(trifluoromethyl sulfonyl)imide salt. The RTIL electrolyte was added in between the solid–solid electrode–electrolyte interfaces and the corresponding performance of the hybrid SSB with CNM/LLZT is shown in Figure S9, Supporting Information. Galvanostatic charge–discharge measurements indicate stable performance over 200 cycles at a current density of 0.3 mA cm^{-2} at 60 °C (Figure S9a, Supporting Information). The coulombic efficiency was found to be lower during the initial cycles, which later improved during cycling. The cell performance was highly stable without any short-circuits indicating the absence of Li dendrite formation. The cell exhibited an average specific capacity of 160.34 mAh g^{-1} with an average coulombic efficiency of 98.65% over 200 cycles. The voltage profile of the cell (Figure S9b, Supporting Information) appeared to be highly stable with low polarization throughout the entire cycle life. The hybrid electrolyte cell with the LLZT (without CNM) only exhibited three cycles before shorting at the fourth cycle during the charging step indicating the propagation of Li dendrites resulting in the short-circuiting of the cell, as shown in Figure S10, Supporting Information. Apart from the short-circuit, the polarization of the cell appeared to continuously increase with cycling probably resulting from the deposition of Li metal within the SSE that hinders the movement of Li-ion transfer across the electrodes.

3. Conclusion

A nanometer thick molecular CNM with sub-nanometer pores was introduced in-between the electrodes and the garnet-type SSE. The CNM, apart from being electronically insulating, regulates the flow of Li-ions into the SSE resulting in a uniform Li-ion flux that suppresses the formation of Li dendrites inside the SSE.

Li plating/stripping using Li–Li symmetrical cell was found to be stable up to a current density of 0.7 mA cm^{-2} with low interfacial resistance. The CNM also increases the adhesion of the electrodes with the SSE, due to the presence of thiol groups, to form an adherent interface. The CNM coated samples were found to be unsusceptible to ambient exposure induced degradation for over 4 weeks of exposure to ambient conditions. The all-solid-state battery using LiFePO$_4$ cathode subjected to over 140 cycles at 0.5 mA cm^{-2} had a capacity retention of 80% with an average coulombic efficiency of 99.82%.

4. Experimental Section

Synthesis of SSE: Stoichiometric quantities of Li$_2$CO$_3$ (20 wt% excess to compensate for the Li loss during sintering), La$_2$O$_3$ (heated at 900 °C for 24 h), ZrO$_2$, and Ta$_2$O$_5$ were thoroughly mixed using a ball mill along with a small quantity of 2-propanol for 6 h. The vacuum-dried mixture was heated at 900 °C for 6 h at a heating and cooling rate of 3 °C min^{-1}. The obtained calcined powder was further ball milled for 24 h along with 2-propanol. The dried powder agglomerates were crushed using a mortar and pestle to obtain fine LLZT powder which was further pressed into pellets using a uniaxial press at 100 MPa pressure. The pellets were sintered at 1160 °C at a heating rate of 2 °C min^{-1} and a cooling rate of 4 °C min^{-1}. Each sintered pellet was polished to about 300 μm thickness in ambient conditions using a polishing machine and then immediately transferred to an argon-filled glove box and dry polished using fine emery (1200 grit) paper to minimize the formation of surface impurities. The final thickness of the pellets was around 260–270 μm.

CNM Synthesis and Transfer: The CNM was synthesized using a well-established technique reported in the previous works.[14b] The starting material for the CNM used for this study was TPT (Sigma-Aldrich, 97%). SAMs of TPT were prepared in an Au/SiO$_2$ substrate. The formed SAMs of TPT molecules were cross-linked by irradiating them using a low energy electron beam (SPECS FG 15/40, 100 eV, 50 mc cm^{-2}) in a high vacuum chamber (<10^{-8} mbar). The formed CNM was coated with a 100 nm supporting layer of PMMA by spin coating. The CNM with the PMMA layer was transferred to the surface polished LLZT pellet using an electrochemical delaminated-assisted transfer process.[28] The transfer was done in such a way that the thiol group of the TPT molecules face the LLZT pellet. The function of the PMMA layer was to protect the CNM from damage during the transfer, shipping, and storage. The PMMA layer was removed prior to the electrochemical cell fabrication by immersing the CNM-coated LLZT in acetone followed by 2-propanol for 10 min each.

Fabrication and Testing of Electrochemical Cells: Symmetric cells were fabricated by sandwiching the CNM/LLZT electrolyte pellets in between two Li foils (Alfa Aesar, 1.5 mm thick) and heating it at 200 °C for 2 h using a hot plate inside the glovebox. Full cells were constructed using a catholyte composition of 60% LiFePO$_4$ cathode powder, 15% conducting carbon, 20% LLZT electrolyte powder, and 5% PVDF binder. The constituents of the catholyte were mixed along with *N*-methyl-2-pyrrolidone (NMP) solvent in a mortar and pestle, and the resultant slurry was drop-casted onto the CNM/LLZT pellet after attaching the Li foil as mentioned in the symmetric cell assembly. The slurry was dried at 40 °C for 48 h under vacuum to obtain a dense catholyte layer and then heated at 90 °C for 8 h to completely evaporate the NMP solvent under a pressure of 2 MPa. Hybrid SSBs were fabricated by adding liquid electrolyte in between the electrode–electrolyte interfaces. 1 M lithium bis(trifluoromethanesulfonyl)imide dissolved in 1-butyl-1-methylpyrrolidinium bis(trifluoromethylsulfonyl)imide was used as the liquid electrolyte. The cathode composition used was composed of LiFePO$_4$, conducting carbon, and PVDF binder in the weight ratio of 80:15:5, mixed using NMP solvent and coated onto the Al foil current collector. The Li foil anode was not subjected to the heating step mentioned previously for the hybrid SSB fabrication. The fabricated cells were transferred to an in-house, custom-built Swagelok-type cell that would apply a stack pressure of 2 MPa. The Swagelok cells were double-sealed using

**ADVANCED
SCIENCE NEWS**

www.advancedsciencenews.com

NANO · MICRO

small

www.small-journal.com

a Teflon tape to prevent any air exposure. All the electrochemical tests were done at 60 °C because of the relatively lower ionic conductivity of LLZT at room temperature.

Materials Characterization and Electrochemical Measurements: XRD (D2 Phaser, Bruker) measurement on LLZT powder was done using a Cu Kα (1.5418 Å) radiation source using a scan rate of $1°$ min^{-1}. Rietveld refinement was performed using GASAS-II software. A reference cif file was obtained from open crystallography database. FE-SEM (JSM 7600, JOEL) images were obtained using an emission current of 15 keV. The XPS analysis was performed using a ThermoFisher Nexsa surface analysis system using a monochromatic Al K_α (1486.6 eV) radiation. Prior to the analysis, the instrument was calibrated using the in-built gold (84.0 eV) and silver (368.2 eV) standards. Post-analysis calibration was performed by assigning the adventitious carbon (C–C bond) peak to 285.0 eV. The obtained spectra were fitted using Gaussian–Lorentzian functions (GL30) in the CasaXPS software. Electrochemical cells were prepared in an Argon-filled glove box (mbraun) with $O_2 < 0.6$ ppm and $H_2O < 0.1$ ppm. EIS was obtained using Biologic SP-200 Potentiostat at a frequency range of 7 MHz to 100 mHz. The electrochemical cells were cycled using an Arbin battery cycler.

Supporting Information

Supporting Information is available from the Wiley Online Library or from the author.

Acknowledgements

Conflict of Interest

S.R., A.G., Z.T., A.T., and L.M.R.A. report a US provisional patent application filed on May 6th, 2020, with a serial number: 63/020,567.

Data Availability Statement

The data that support the findings of this study are available from the corresponding author upon reasonable request.

Keywords

[1] a) S. Lv, T. Verhallen, A. Vasileiadis, F. Ooms, Y. Xu, Z. Li, Z. Li, M. Wagemaker, *Nat. Commun.* **2018**, *9*, 1; b) Y. Gao, Y. Zhao, Y. C. Li, Q. Huang, T. E. Mallouk, D. Wang, *J. Am. Chem. Soc.* **2017**, *139*, 15288.

[2] a) K. Park, B.-C. Yu, J.-W. Jung, Y. Li, W. Zhou, H. Gao, S. Son, J. B. Goodenough, *Chem. Mater.* **2016**, *28*, 8051; b) G. Cui, *Matter* **2020**, *2*, 805; c) D. Gopalakrishnan, S. Alkatie, A. Cannon, S. Rajendran, N. K. Thangavel, N. Bhagirath, E. M. Ryan, L. M. R. Arava, *Sustainable Energy Fuels* **2021**, *5*, 1488; d) V. Mullaivananathan, R. Sathish, N. Kalaiselvi, *Electrochim. Acta* **2017**, *225*, 143.

[3] a) A. Manthiram, X. Yu, S. Wang, *Nat. Rev. Mater.* **2017**, *2*, 16103; b) S. Rajendran, N. K. Thangavel, K. Mahankali, L. M. R. Arava, *ACS Appl. Energy Mater.* **2020**, *3*, 6775.

[4] a) T. Famprikis, P. Canepa, J. A. Dawson, M. S. Islam, C. Masquelier, *Nat. Mater.* **2019**, *18*, 1278; b) Q. Zhao, S. Stalin, C.-Z. Zhao, L. A. Archer, *Nat. Rev. Mater.* **2020**, *5*, 229.

[5] a) C. Wang, K. Fu, S. P. Kammampata, D. W. McOwen, A. J. Samson, L. Zhang, G. T. Hitz, A. M. Nolan, E. D. Wachsman, Y. Mo, *Chem. Rev.* **2020**, *120*, 4257; b) V. Thangadurai, S. Narayanan, D. Pinzaru, *Chem. Soc. Rev.* **2014**, *43*, 4714.

[6] Y. Xiao, Y. Wang, S.-H. Bo, J. C. Kim, L. J. Miara, G. Ceder, *Nat. Rev. Mater.* **2020**, *5*, 105.

[7] a) K. Tantratian, H. Yan, K. Ellwood, E. T. Harrison, L. Chen, *Adv. Energy Mater.* **2021**, *11*, 2003417; b) E. Kazyak, R. Garcia-Mendez, W. S. LePage, A. Sharafi, A. L. Davis, A. J. Sanchez, K.-H. Chen, C. Haslam, J. Sakamoto, N. P. Dasgupta, *Matter* **2020**, *2*, 1025.

[8] J. E. Ni, E. D. Case, J. S. Sakamoto, E. Rangasamy, J. B. Wolfenstine, *J. Mater. Sci.* **2012**, *47*, 7978.

[9] a) R. Koerver, W. Zhang, L. de Biasi, S. Schweidler, A. O. Kondrakov, S. Kolling, T. Brezesinski, P. Hartmann, W. G. Zeier, J. Janek, *Energy Environ. Sci.* **2018**, *11*, 2142; b) T. Shi, Y.-Q. Zhang, Q. Tu, Y. Wang, M. Scott, G. Ceder, *J. Mater. Chem. A* **2020**, *8*, 17399.

[10] F. Han, A. S. Westover, J. Yue, X. Fan, F. Wang, M. Chi, D. N. Leonard, N. J. Dudney, H. Wang, C. Wang, *Nat. Energy* **2019**, *4*, 187.

[11] C. Ma, Y. Cheng, K. Yin, J. Luo, A. Sharafi, J. Sakamoto, J. Li, K. L. More, N. J. Dudney, M. Chi, *Nano Lett.* **2016**, *16*, 7030.

[12] H. Huo, J. Luo, V. Thangadurai, X. Guo, C.-W. Nan, X. Sun, *ACS Energy Lett.* **2019**, *5*, 252.

[13] Z. Cheng, M. Liu, S. Ganapathy, C. Li, Z. Li, X. Zhang, P. He, H. Zhou, M. Wagemaker, *Joule* **2020**, *4*, 1311.

[14] a) A. Turchanin, A. Golzhauser, *Adv. Mater.* **2016**, *28*, 6075; b) P. Angelova, H. Vieker, N.-E. Weber, D. Matei, O. Reimer, I. Meier, S. Kurasch, J. Biskupek, D. Lorbach, K. Wunderlich, *ACS Nano* **2013**, *7*, 6489.

[15] C. Neumann, R. A. Wilhelm, M. Küllmer, A. Turchanin, *Faraday Discuss.* **2021**, *227*, 61.

[16] a) Y. Yang, P. Dementyev, N. Biere, D. Emmrich, P. Stohmann, R. Korzetz, X. H. Zhang, A. Beyer, S. Koch, D. Anselmetti, A. Golzhauser, *ACS Nano* **2018**, *12*, 4695; b) Y. Yang, R. Hillmann, Y. B. Qi, R. Korzetz, N. Biere, D. Emmrich, M. Westphal, B. Buker, A. Hutten, A. Beyer, D. Anselmetti, A. Golzhauser, *Adv. Mater.* **2020**, *32*, 1907850.

[17] S. Rajendran, Z. Tang, A. George, A. Cannon, C. Neumann, A. Sawas, E. Ryan, A. Turchanin, L. M. R. Arava, *Adv. Energy Mater.* **2021**, *11*, 2100666.

[18] K. Kataoka, J. Akimoto, *J. Ceram. Soc. Jpn.* **2019**, *127*, 521.

[19] K. Kataoka, J. Akimoto, *ChemElectroChem* **2018**, *5*, 2551.

[20] R. Wagner, G. N. J. Redhammer, D. Rettenwander, G. Tippelt, A. Welzl, S. Taibl, J. R. Fleig, A. Franz, W. Lottermoser, G. Amthauer, *Chem. Mater.* **2016**, *28*, 5943.

[21] K. K. Fu, Y. Gong, B. Liu, Y. Zhu, S. Xu, Y. Yao, W. Luo, C. Wang, S. D. Lacey, J. Dai, *Sci. Adv.* **2017**, *3*, e1601659.

[22] S. Rajendran, A. Pilli, O. Omolere, J. Kelber, L. M. R. Arava, *Chem. Mater.* **2021**, *33*, 3401.

[23] A. Sharafi, S. Yu, M. Naguib, M. Lee, C. Ma, H. M. Meyer, J. Nanda, M. Chi, D. J. Siegel, J. Sakamoto, *J. Mater. Chem. A* **2017**, *5*, 13475.

[24] M. Herstedt, D. P. Abraham, J. B. Kerr, K. Edström, *Electrochim. Acta* **2004**, *49*, 5097.

ADVANCED
SCIENCE NEWS

www.advancedsciencenews.com

NANO · MICRO
small
www.small-journal.com

[25] L. Cheng, C. H. Wu, A. Jarry, W. Chen, Y. Ye, J. Zhu, R. Kostecki, K. Persson, J. Guo, M. Salmeron, *ACS Appl. Mater. Interfaces* **2015**, *7*, 17649.

[26] T. Ishida, W. Mizutani, H. Azehara, K. Miyake, Y. Aya, S. Sasaki, H. Tokumoto, *Surf. Sci.* **2002**, *514*, 187.

[27] P. Penner, X. Zhang, E. Marschewski, F. Behler, P. Angelova, A. Beyer, J. Christoffers, A. Gölzhäuser, *J. Phys. Chem. C* **2014**, *118*, 21687.

[28] Z. Tang, C. Neumann, A. Winter, A. Turchanin, *Nanoscale* **2020**, *12*, 8656.

[29] E. Griffin, L. Mogg, G.-P. Hao, G. Kalon, C. Bacaksiz, G. Lopez-Polin, T. Zhou, V. Guarochico, J. Cai, C. Neumann, *ACS Nano* **2020**, *14*, 7280.

[30] Y. Yang, P. Dementyev, N. Biere, D. Emmrich, P. Stohmann, R. Korzetz, X. Zhang, A. Beyer, S. Koch, D. Anselmetti, *ACS Nano* **2018**, *12*, 4695.

[31] V. Stroganov, D. Hüger, C. Neumann, T. Noethel, M. Steinert, U. Huebner, A. Turchanin, *Small* **2023**, 2300282.

[32] J. C. Jones, S. Rajendran, A. Pilli, V. Lee, N. Chugh, L. M. R. Arava, J. A. Kelber, *J. Vac. Sci. Technol., A* **2020**, *38*, 023201.

[33] X. Zhang, A. Beyer, *Nanoscale* **2021**, *13*, 1443.

[34] S. Patra, B. R. V. Krupa, S. Chakravarty, R. Murugan, *Electrochim. Acta* **2019**, *312*, 320.

[35] X. Liu, X. Li, H. Li, H. B. Wu, *Chem. - Eur. J.* **2018**, *24*, 18293.

2303625 (10 of 10)